3-D Printed Transmission-Reflection-Integrated Metasurface for Spin-Decoupled Full-Space Quadruplex Channels Independent Phase Modulation

Jianfeng Zhu, *Member, IEEE*, Yang Yang, *Senior Member, IEEE*

***Abstract*—This article demonstrates 3-D printed transmission-reflection-integrated (TRI) metasurfaces (MSs), which achieve full-space spin-decoupled channels with independent phase modulation. Under a circularly polarized (CP) incident wave illumination, the phase of left-hand circularly polarized (LHCP) and right-hand circularly polarized (RHCP) channels in the reflecting and transmitting spaces can be independently controlled. The meta-atom comprises linearly polarized (LP) patches at the top and bottom with phase delay lines connecting them. In the reflecting space, varying the size of the LP patch provides the same dynamic phase-shifting for the LHCP and RHCP channels. Meanwhile, globally rotating the meta-atom introduces Pancharatnam–Berry (P-B) phase-shifting for the reflected co-polarization channel. Thus, the LHCP and RHCP channels in the reflecting space can be fully decoupled. As for the transmitting space, the phase delay lines provide the same dynamic phase-shifting for the LHCP and RHCP channels. Meanwhile, locally rotating the transmitting antenna provides opposite geometric phase-shifting for the LHCP and RHCP channels. Thus, the LHCP and RHCP channels in the transmitting space can be decoupled as well. To demonstrate, different TRI MSs achieving quadruplex channel multiplexing under CP wave illuminations are simulated and experimentally verified.**

***Index Terms*— 3-D printing, full space, spin-decoupled, TRI metasurface.**

I. INTRODUCTION

Metasurfaces (MSs) are planar composite periodic or semi-periodic subwavelength scale structures that have an unprecedented ability to manipulate electromagnetic wave, enabling functionalities beyond what conventional device provides [1], [2], [3], [4]. They introduce strong wave-matter interactions and completely control the wave properties, including phase, amplitude, and polarization, leading to many functional devices with compact form factors, such as wireless power transfer devices [5], [6], [7], meta-lens [8], [9], [10], [11], [12], [13], [14], [15], [16], [17], [18], [19], meta-hologram [20], [21], [22], [23], [24], [25], [26], [27] and many other [28], [29]. Multi-channel MSs, combining several degrees of freedom, such as polarization, wavelength, and spatial modulation, to achieve diverse functionalities, have drawn considerable attention. For example, by combining dynamic and Pancharatnam-Berry (P-B) phases, plenty of spin-decoupled beam-shaping functional devices were designed for various applications [30], [31], [32], [33], [34], [35], [36], [37], [38], [39]. With the assistance of the chirality phase, transmissive MS that controls the co-polarization and cross-polarization of the left-hand circularly polarized (LHCP) and right-hand circularly polarized (RHCP) incident waves was demonstrated to increase the MS's information capacity [40]. Later, spin-decoupled transmissive MS with polarization preserving feature was demonstrated by combining the chirality phase and dynamic phase [41], [42]. However, the function of the above-mentioned MSs was limited to half-space, i.e., transmitting or reflecting space.

With the rise of reconfigurable intelligent surface (RIS), transmission-reflection-integrated (TRI) MS-aided communication has received growing interest [39], [40], [41], [42], [43], [44], [45], [46]. TRI-aided communication has been recognized as a new approach to improve the flexibility and effectiveness of the RIS system [47], [48], [49], [50]. In contrast to reflecting-only RISs, each meta-atom of TRI-RISs transmits and reflects the input signal simultaneously, enlarging the beam coverage and breaking the geographical limitations for the RIS deployment, as depicted in Fig. 1. Therefore, the key for TRI-

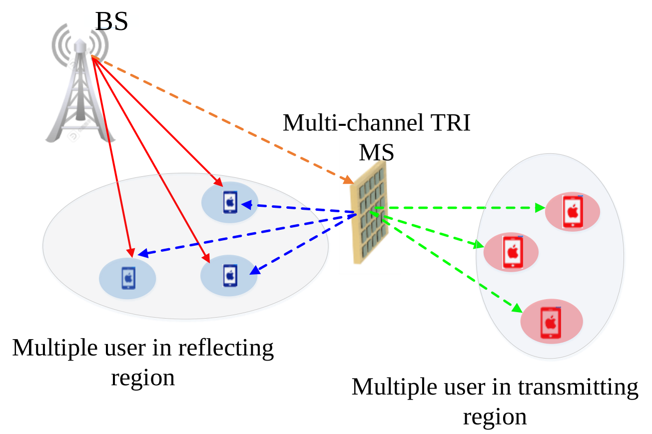

Fig. 1. Multi-channel TRI MS aided wireless network.

This work was supported by the Nano Dimension through collaborative projects, in part by the Australian Research Council—ARC Linkage Projects under Grant LP210300004, the ARC Linkage Infrastructure under Grant LE220100035, and the National Natural Science Foundation of China under Grant 62301225. (*Corresponding author: Yang Yang*.)

Jianfeng Zhu is with Guangdong Principle Key Laboratory of Millimeter-wave and Terahertz, School of Electronic and Information Engineering, South China University of Technology, Guangzhou 510641, China.

Yang Yang is with school of Electrical and Data Engineering, University of Technology Sydney, Ultimo, NSW 2007, Australia.

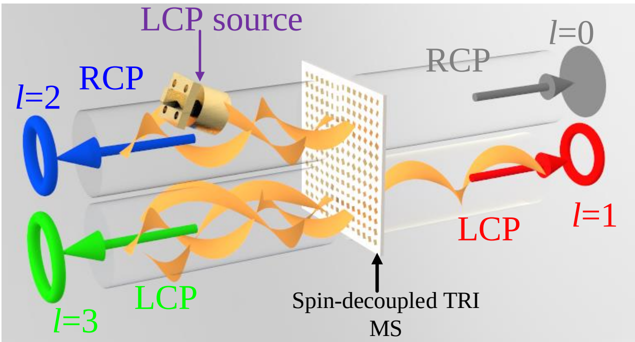

Fig. 2. Schematic of the full-space spin-decoupled TRI MS supporting independent quadruplex channels carry OAM with topological charges of 0, 1, 2, 3.

aided communication lies in the successful implementation of the TRI MS. Till now, several TRI MSs have been reported. A microwave TRI MS was demonstrated, which reflects the *y*-polarized incident wave and allows the *x*-polarized incident wave to pass [42]. Hence, the function can be switched by changing the polarization of the linearly polarized (LP) incident wave. The programmable TRI MSs were also demonstrated by integrating PIN diodes [43]. Nevertheless, they only operate under LP incidence. Compared to LP, CP radiation is more desirable in communication systems since the CP wave can avoid polarization mismatch. However, the emergence of full-space spin-decoupled multi-channel MSs still remains elusive and in its infancy. Ultrathin broadband single-layer MSs are demonstrated to work simultaneously in transmitting and reflecting spaces under CP wave illumination [46]. However, only the cross-polarization channel in transmitting space and the co-polarization channel in reflecting space can be controlled. Thus, the ultimate barrier to achieving independent wavefront-shaping in co-polarization and cross-polarization in full space is still unconquered.

This article demonstrates 3-D printed TRI MSs, which achieve full-space spin-decoupled channels with independent phase modulation in millimeter wave region. Under CP incident wave illumination, the phase distributions of LHCP and RHCP channels in the reflecting and transmitting space can be independently manipulated. A schematic view of the full-space spin-decoupled TRI MS is illustrated in Fig. 2. As an example, under LHCP incident wave, the MS can redistribute energy into the four channels and achieves orbit angular momenta (OAM) with topological charges of 0 (transmitting space, RHCP channel), 1 (transmitting space, LHCP channel), 2 (reflecting space, RHCP channel), 3 (reflecting space, LHCP channel). Several MSs achieving different wavefronts in quadruplex channels under LHCP and RHCP wave illuminations are simulated and experimentally verified. The MSs are conveniently fabricated using the multi-material 3-D printing technique.

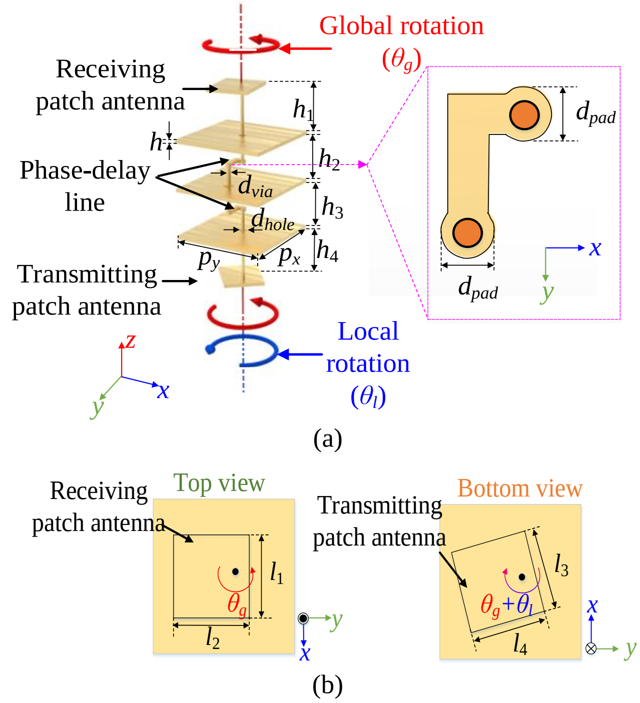

Fig. 3. (a) Geometry and dimensions of the meta-atom. (b) Top view and bottom view of the meta-atom. (Px=5.4 mm, Py=5.4 mm, h=0.035mm, h_1=0.47mm, h_2=0.435mm, h_3=0.435mm, h_4=0.47mm, l_2 =2.88 mm, l_3 =2.8 mm, l_4 =2.88 mm, d_{via}=0.2 mm, d_{hole}=0.35 mm. d_{pad}=0.32 mm)

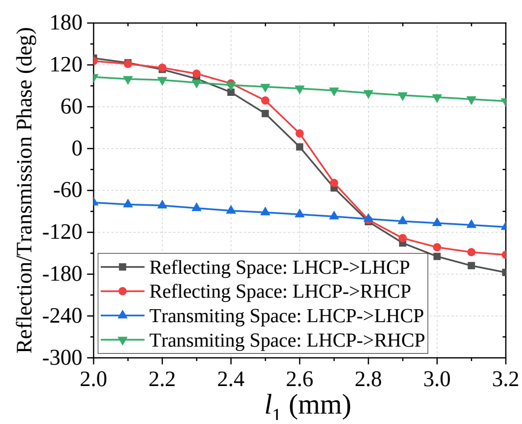

Fig. 4. Transmission/reflection phase of the LHCP and RHCP channels by varying the values of l_1 under LHCP incident wave.

II. Meta-Atom Design and Principle

The meta-atom consists of an LP patch on the top and bottom as the receiving and transmitting antenna with phase delay lines connecting them, as depicted in Fig. 3. Seven conductive layers in total are used to form the meta-atom. The thickness of the conductor layer is 35 μm (h), and the total thickness of the meta-atom is 1.985 mm. The conductor layers are printed using nanoparticle silver ink, while the dielectric layer is printed using acrylate ink (ε_r=2.8, loss tangent=0.012) to support the multiple conductor layers. In the reflecting space, varying the size of the patch provides the same dynamic phase-shifting for

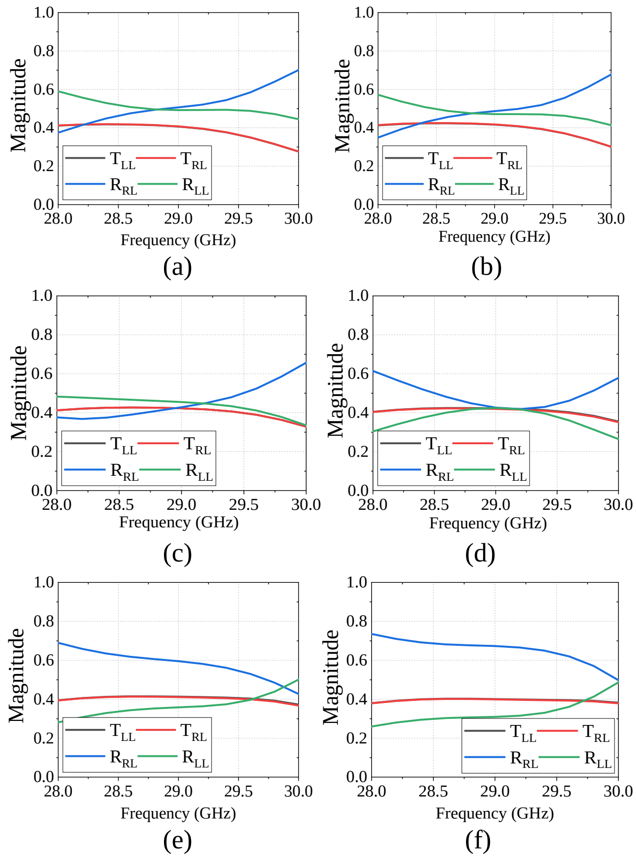

Fig. 5. Transmission and reflection magnitude in the four channels under LHCP incident wave when the length of l_1 is varied. a) l_1=3.2mm, b) l_1=3.0mm, c) l_1=2.8mm, d) l_1=2.6mm, e) l_1=2.4mm, f) l_1=2.2mm. in the legend, T and R represent transmitted and reflected modes, and subscript LL/RL represent LHCP input to LHCP/RHCP output, respectively.)

both LHCP and RHCP channels. Globally rotating the meta-atom introduces P-B phase-shifting for the reflected co-polarization channel. Thus, the LHCP and RHCP channels can be decoupled. In contrast, the phase delay lines provide the same dynamic phase-shifting for the LHCP and RHCP channels in the transmitting space. Meanwhile, locally rotating the transmitting antenna introduces the chirality phase, providing opposite phase-shifting for the LHCP and RHCP channels. Hence, the LHCP and RHCP channels in the transmitting space are decoupled by combining the dynamic and chirality phases. Assuming CP incident wave, the linearly polarized patch antenna receives the *y*-polarized component and reflects the *x*-polarized component of the incident wave. Thus, in the reflecting space, the reflective Jones matrix can be expressed as:

$$R=\begin{bmatrix} R_{xx} & R_{xy} \\ R_{yx} & R_{yy} \end{bmatrix}=\begin{bmatrix} e^{j\varphi_R} & 0 \\ 0 & 0 \end{bmatrix}. \tag{1}$$

The phase-shifting φ_R is achieved by changing the length of the patch (l_1) due to the patch resonance along *x*-direction. Meanwhile, through globally rotating the meta-atom (θ_g), the effect can be expressed as:

$$\begin{aligned} R(\theta_g) &= S^{-1}(\theta_g)\cdot R\cdot S(\theta_g) \\ &=\begin{bmatrix} \cos\theta_g & -\sin\theta_g \\ \sin\theta_g & \cos\theta_g \end{bmatrix}\begin{bmatrix} e^{j\varphi_R} & 0 \\ 0 & 0 \end{bmatrix}\begin{bmatrix} \cos\theta_g & \sin\theta_g \\ -\sin\theta_g & \cos\theta_g \end{bmatrix}. \end{aligned} \tag{2}$$

Considering the LHCP ($|L\rangle$=[1, j]/$\sqrt{2}$ and RHCP ($|R\rangle$=[1, -j]/$\sqrt{2}$) as the incident wave, the output E-fields in the reflecting space can be expressed as:

LHCP:

$$\begin{aligned} E_R^{out} &= R(\theta_g)\cdot\frac{\sqrt{2}}{2}\cdot\begin{bmatrix} 1 \\ i \end{bmatrix} \\ &=\frac{\sqrt{2}}{4}\cdot e^{j\varphi_R}\cdot\begin{bmatrix} 1 \\ i \end{bmatrix}+\frac{\sqrt{2}}{4}\cdot e^{j\varphi_R}\cdot e^{j2\cdot\theta_g}\cdot\begin{bmatrix} 1 \\ -i \end{bmatrix} \end{aligned} \tag{3-1}$$

RHCP:

$$\begin{aligned} E_R^{out} &= R(\theta_g)\cdot\frac{\sqrt{2}}{2}\cdot\begin{bmatrix} 1 \\ -i \end{bmatrix} \\ &=\frac{\sqrt{2}}{4}\cdot e^{j\varphi_R}\cdot e^{-j2\cdot\theta_g}\cdot\begin{bmatrix} 1 \\ i \end{bmatrix}+\frac{\sqrt{2}}{4}\cdot e^{j\varphi_R}\cdot\begin{bmatrix} 1 \\ -i \end{bmatrix} \end{aligned} \tag{3-2}$$

As seen from equation (3), the reflected wave can be equally decomposed into LHCP and RHCP components. Meanwhile, for the LHCP incident waves, the reflected RHCP component's phase-shifting solely depends on the φ_R, and the phase-shifting of the reflected LHCP component depends on the φ_R and the global rotation angle θ_g. It is understood that varying the patch size along the *x*-direction provides the same dynamic phase for the LHCP and RHCP components. Globally rotating the meta-atom introduces the P-B phase, where the phase-shifting only exists when the spin flips, *i.e.*, LHCP input to the reflected LHCP output (note that the propagation direction is reversed in the reflecting space). Similarly, for the RHCP incident wave, the phase-shifting of the reflected LHCP component solely depends on the φ_R, and the reflected RHCP component depends on the φ_R and the global rotation angle θ_g, as shown in equation (3-2).

As for the transmitting space, the patch antenna receives the *y*-polarized component of the CP wave and induces this part of energy into the patch antenna on the transmitting side. Therefore, the transmissive Jones matrix can be expressed as:

$$T=\begin{bmatrix} T_{xx} & T_{xy} \\ T_{yx} & T_{yy} \end{bmatrix}=\begin{bmatrix} 0 & 0 \\ 0 & e^{j\varphi_T} \end{bmatrix}. \tag{4}$$

where the phase-shifting φ_T is obtained by varying the length of the phase delay line. The patch antenna in the transmitting side rotates locally with an angle of θ_l. Then, the Jones matrix can be expressed as:

$$T(\theta_l)=\begin{bmatrix} \cos\theta_l & -\sin\theta_l \\ \sin\theta_l & \cos\theta_l \end{bmatrix}\cdot T. \tag{5}$$

Meanwhile, the meta-atom also globally rotates with a global rotation angle of θ_g, the Jones matrix can be written as:

$$T(\theta_l,\theta_g)=S^{-1}(\theta_g)\cdot T(\theta_l)\cdot S(\theta_g). \tag{6}$$

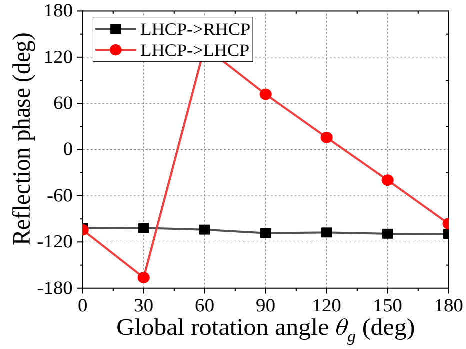

(a)

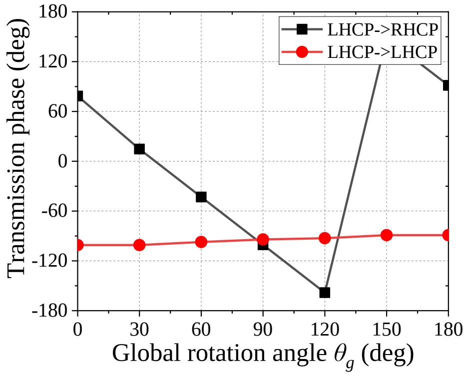

(b)

Fig. 6. (a) Reflection phase of LHCP and RHCP channels by globally rotating the meta-atom under LHCP incident wave. (b) Transmission phase of LHCP and RHCP channels by globally rotating the meta-atom under LHCP incident wave.

Considering the LHCP (RHCP) as the incident wave, the E-fields in the transmitting space can be expressed as:
LHCP:

$$E_T^{out} = T(\theta_l,\theta_g)\cdot\frac{\sqrt{2}}{2}\cdot\begin{bmatrix}1\\ i\end{bmatrix}$$
$$=\frac{\sqrt{2}}{4}\cdot e^{j\varphi_T}\cdot e^{-j\theta_l}\cdot\begin{bmatrix}1\\ i\end{bmatrix}+\frac{\sqrt{2}}{4}\cdot e^{j\varphi_T}\cdot e^{j\theta_l}\cdot e^{j2\theta_g}\cdot e^{j\pi}\cdot\begin{bmatrix}1\\ -i\end{bmatrix} \quad (7\text{-}1)$$

RHCP:

$$E_T^{out} = T(\theta_l,\theta_g)\cdot\frac{\sqrt{2}}{2}\cdot\begin{bmatrix}1\\ -i\end{bmatrix}$$
$$=\frac{\sqrt{2}}{4}\cdot e^{j\varphi_T}\cdot e^{j\theta_l}\cdot\begin{bmatrix}1\\ -i\end{bmatrix}+\frac{\sqrt{2}}{4}\cdot e^{j\varphi_T}\cdot e^{-j\theta_l}\cdot e^{-j2\theta_g}\cdot e^{j\pi}\cdot\begin{bmatrix}1\\ i\end{bmatrix} \quad (7\text{-}2)$$

As seen from equation (7), varying the length of the phase delay line provides phase-shifting φ_T for both the LHCP and RHCP channels. Meanwhile, locally rotating the transmitting antenna provides opposite phase-shifting for the LHCP and RHCP channels. It is worth mentioning that globally rotating the meta-atom also introduces phase-shifting for the cross-polarization channel in the transmitting space because of the P-B phase. However, the global rotation angle (θ_g) has already been determined for decoupling the LHCP and RHCP channels in reflecting space. Therefore, only the dynamic phase and the local rotation angle are used to decouple the LHCP and RHCP in transmitting space.

The performance of the meta-atom is simulated in Ansys. HFSS. The reflection phase by varying the size of the receiving patch (l_1) is shown in Fig. 4. Near 310° dynamic phase is obtained for both the LHCP and RHCP channels when the values of l_1 vary from 2 mm to 3.2 mm at 29-GHz. Meanwhile, the transmission phase shifting is less than 40° when the values of l_1 vary from 2 mm to 3.2 mm. The transmitted and reflected magnitude of LHCP and RHCP channels of different values of l_1 is also investigated in Fig. 5. Because the magnitudes of the T_{RL} and T_{LL} are the same, the two curves are overlapped in Fig. 5. In addition, it is observed that the energy is nearly equally distributed into the four channels at the center frequency when the l_1 is adjusted from 3.2mm to 2.6mm. However, the reflection magnitude difference between the R_{LL} and R_{RL} gradually increases when the l_1 is further reduced to 2.2mm. This is because when the value of the l_1 is further reduced, the impedance matching of the receiving antenna deteriorates. Thus, more energy is reflected, resulting in the power unequally distributed in the four channels.

The reflected LHCP and RHCP channels phases when the meta-atom is globally rotated are shown in Fig. 6(a). The phase-shifting values of the reflected co-polarization (LHCP) channel are twice the rotation angle, while the phase-shifting of the reflected cross-polarization channel (RHCP) is constant. The

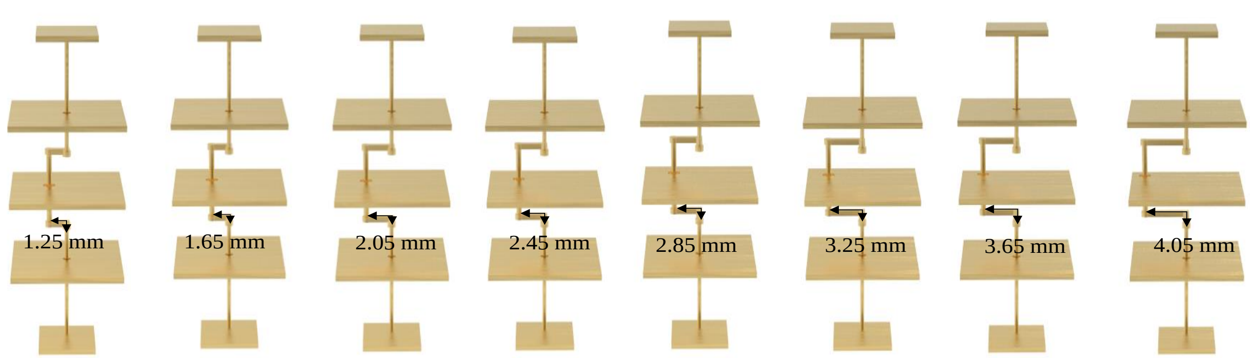

I II III IV V VI VII VIII

Fig. 7. Configuration and dimensions of eight-level meta-atoms. Other parameters are the same as the one in Fig. 2.

TABLE I
AMPLITUDE AND PHASE RESPONSE OF THE EIGHT-LEVEL META-ATOM AT 29GHZ

Meta-atom	I	II	III	IV	V	VI	VII	VIII
	Mag/Phase	Mag/Phase	Mag/Phase	Mag/Phase	Mag/Phase	Mag/Phase	Mag/Phase	Mag/Phase
T_{RL}	0.43/-8°	0.41/-49°	0.43/-102°	0.38/-158°	0.34/153°	0.36/115°	0.38/72°	0.40/20°
T_{LL}	0.43/173°	0.41/131°	0.43/78°	0.38/21°	0.34/-25°	0.36/-64°	0.38/-107°	0.40/-150°

transmitted LHCP and RHCP channel phases when the meta-atom is globally rotated are shown in Figure. 6 (b). The phase-shifting values of the transmitted cross-polarization channel (RHCP) are twice the rotation angle, while the phase-shifting of transmitted co-polarization channel (LHCP) is constant.

The lengths of the phase delay lines are adjusted to introduce the same dynamic phase-shifting (φ_T) for the transmitted LHCP and RHCP channels. Eight-level meta-atoms, marked as I to VIII, are adopted to cover the 2π dynamic phase-shifting. The phase delay line's lengths are provided in Fig. 7. The corresponding transmission magnitude and phase at 29-GHz are summarized in Table I. In addition, the phase response is stable under oblique incident with an angle up to 40°. The transmitted phases of the LHCP and RHCP channels of the eight-level meta-atom at 29GHz are also plotted in Fig. 8 (a). As can be seen, the phase delay lines provide the same dynamic phase for

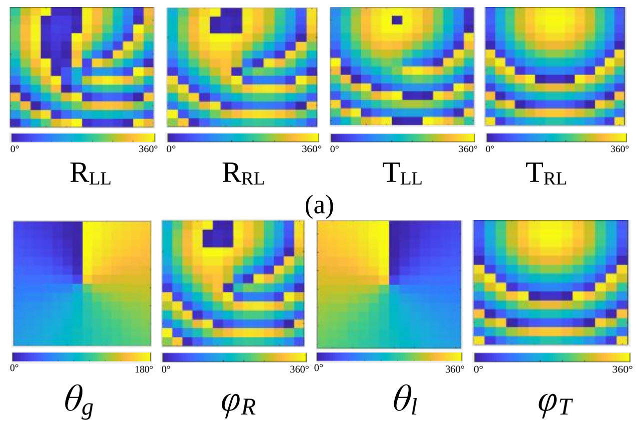

Fig. 9. (a) Compensating phase masks of R_{LL}, R_{RL}, T_{LL} and T_{RL} channels. (b) Phase masks of θ_g, φ_R, θ_l, φ_T.

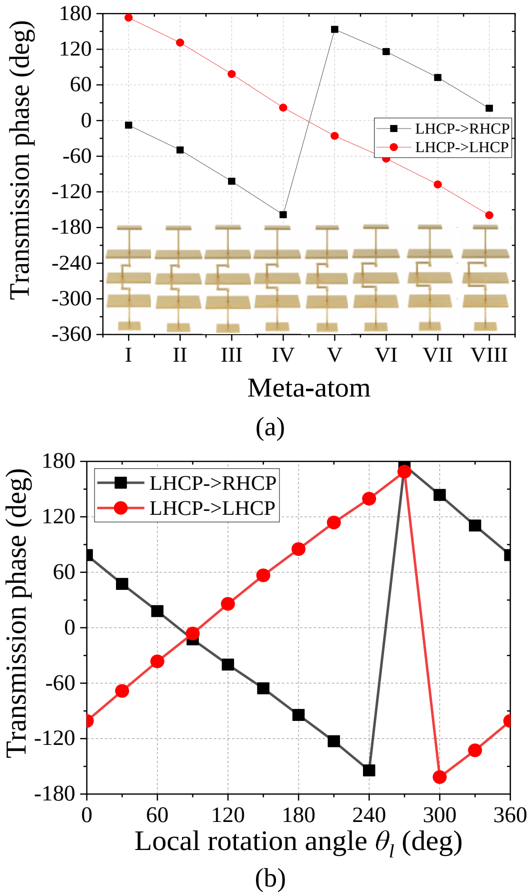

Fig. 8. (a) Transmission phase of LHCP and RHCP channels at 29 GHz of the eight-level meta-atom under LHCP incident wave. (b) Transmission phase of LHCP and RHCP channels when the transmitting antenna is locally rotated under LHCP incident wave.

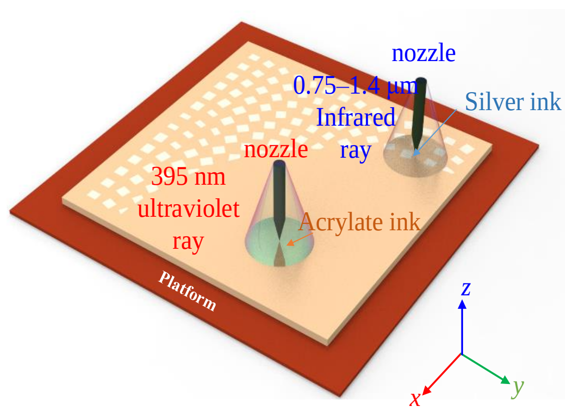

Fig. 10. The sample under fabrication using multi-materials-integrated 3-D printing technique.

the transmitted LHCP and RHCP channels. The phase-shifting of the transmitted LHCP and RHCP channels when the transmitting antenna is locally rotated is given in Fig. 8 (b). It is observed that the transmitted absolute phase-shifting of the LHCP and RHCP channels are equal to the rotation angle of the transmitting antenna (θ_l) whereas the tendencies are opposite.

III. MS DESIGN, FABRICATION AND MEASUREMENT

Different MSs achieving full-space quadruplex channel multiplexing under LHCP and RHCP wave illumination are designed and measured for demonstration.

A. LHCP Input

Two TRI MSs are designed to achieve spin-decoupled full space quadruplex channels independent beam shaping under LHCP incident wave. The MS must provide four uncorrelated phase profiles, namely, $R_{LL}(x,y)$ and $R_{RL}(x,y)$ for the reflected

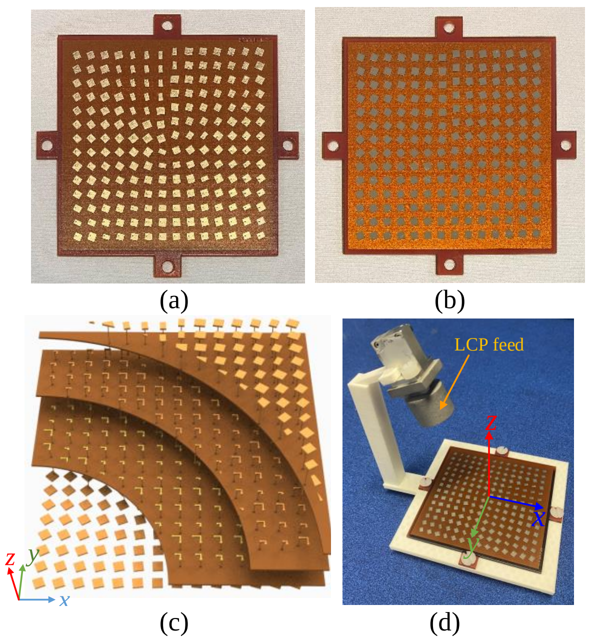

Fig. 11. (a) Front view of the sample. (b) Back view of the sample. (c) Internal view. (d) Assembling view.

co-polarization and cross-polarization channels, and $T_{LL}(x,y)$ and $T_{RL}(x,y)$ for the transmitted co-polarization and cross-polarization channels, respectively. Based on Equations (3-1) and (7-1), φ_R, θ_g, θ_l, φ_T can be calculated as:

$$\varphi_R(x,y)=R_{RL}(x,y). \quad (8)$$

$$\varphi_R(x,y)+2\cdot\theta_g(x,y)=R_{LL}(x,y). \quad (9)$$

$$\varphi_T(x,y)-\theta_l(x,y)=T_{LL}(x,y). \quad (10)$$

$$\varphi_T(x,y)+\theta_l(x,y)+2\cdot\theta_g(x,y)=T_{RL}(x,y). \quad (11)$$

The first MS collimates the wave from the LHCP feed and produces vortex beams with different modes (l) for the four channels. Specifically, l=0, 1, 2, 3 for the T_{RL}, T_{LL}, R_{RL}, and R_{LL} channels, respectively. The LHCP feed is placed at (x=-30mm, y=0mm, and z=70mm). The phase profile of R_{LL}, R_{RL}, T_{LL}, and T_{RL} can be written as:

$$R_{LL}(x,y)=k\cdot\vec{R}_i+3\cdot\varphi \quad R_{RL}(x,y)=k\cdot\vec{R}_i+2\cdot\varphi. \quad (12)$$

$$T_{LL}(x,y)=k\cdot\vec{R}_i+1\cdot\varphi \quad T_{RL}(x,y)=k\cdot R_i+0\cdot\varphi. \quad (13)$$

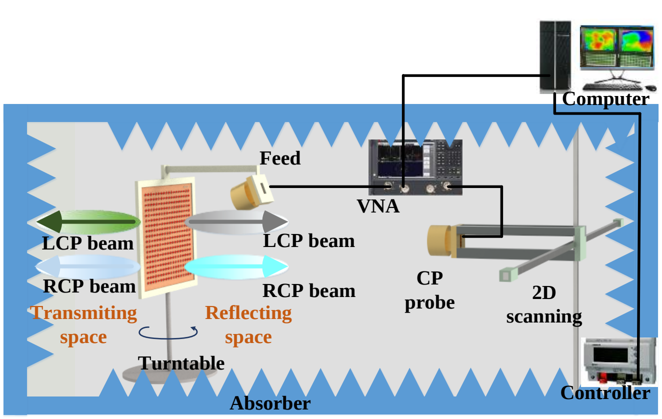

Fig. 12. Near-field measurement setup.

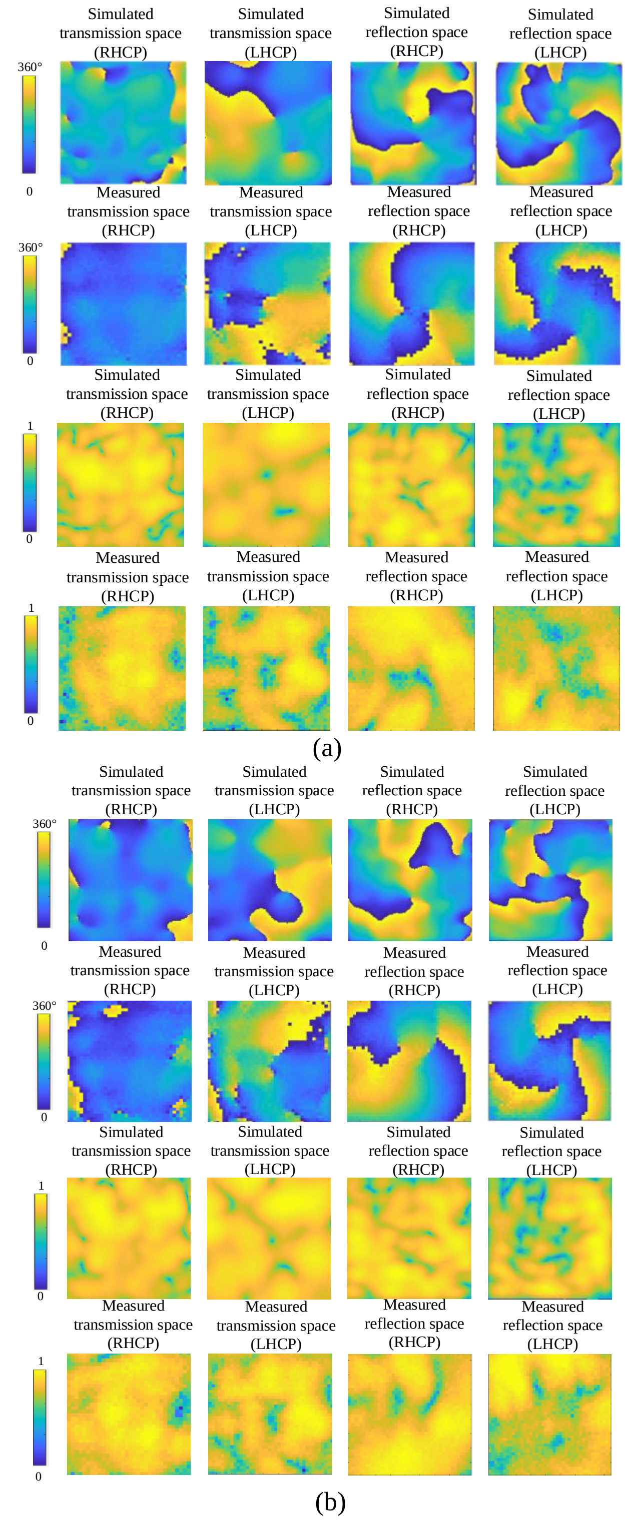

Fig. 13. Simulated and measured phase and intensity profiles (normalized) of LHCP and RHCP channels in the transmitting and reflecting spaces. (a) 29 GHz. (b) 29.5 GHz.

where k is the wavenumber in free space. R_i represents the distance between the MS's i^{th} element and the feed. φ is the azimuthal angle around the beam axis. The phase masks of R_{LL}, R_{RL}, T_{LL}, and T_{RL} are shown in Fig. 9 (a). Based on equations (8) to (11), the φ_R, θ_g, θ_l, φ_T can be calculated as:

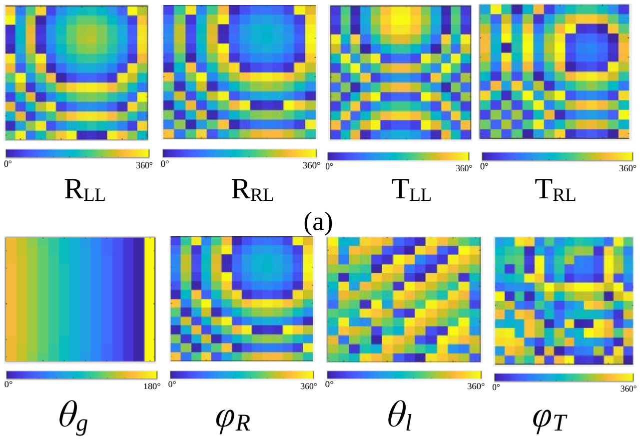

Fig. 14. a) Compensating phase masks of R_{LL}, R_{RL}, T_{LL} and T_{RL} channels. b) Phase masks of $\theta_g, \varphi_R, \theta_l, \varphi_T$.

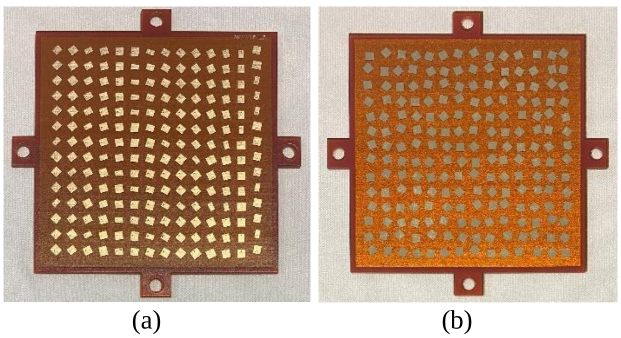

Fig. 15. (a) Front view of the sample. (b) Back view of the sample.

$$\varphi_R(x,y) = R_{RL}(x,y) \quad (14)$$

$$\theta_g(x,y) = 0.5\cdot(R_{LL} - R_{RL}) \quad (15)$$

$$\theta_l(x,y) = 0.5\cdot(T_{RL} - T_{LL} + R_{RL} - R_{LL}) \quad (16)$$

$$\varphi_T(x,y) = 0.5\cdot(T_{RL} + T_{LL} + R_{RL} - R_{LL}) \quad (17)$$

The corresponding phase masks for the φ_R, θ_g, θ_l, φ_T on the MS aperture are shown in Fig. 9 (b). 14×14 elements in total are used to form the MS and the MS is conveniently fabricated using 3-D printing. During printing, a 0.75–1.4 μm near-infrared radiation (NIR) lamp is turned on to sinter the silver ink to form the conductor layers. In contrast, a 395 nm UV lamp is utilized to sinter the acrylate ink to realize the dielectric layer, as illustrated in Fig. 10. The prototype is shown in Fig. 11. As for the measurement, the LHCP feed horns illuminate the samples under test, and the LHCP and RHCP probes are respectively located in the transmitting and reflecting space to record the power and phase, as depicted in Fig. 12. During the measurement, 1600 pixels in total are used to capture the magnitude and phase information of the MS with a scanning area of 120 mm×120 mm. The simulated and measured phase and intensity profile of transmitted and reflected LHCP and RHCP channels are given in Fig. 13. The measured results agree with the simulated ones. The modes of 0 (plane wave), 1, 2, and 3 can be clearly observed for the transmitted co-polarization, transmitted cross-polarization, reflected cross-polarization, and reflected co-polarization, respectively. The mode purities at 29 GHz is 87%, 89%, 89% and 78% for the mode 0, 1, 2 and 3, respectively. The intensity profiles have

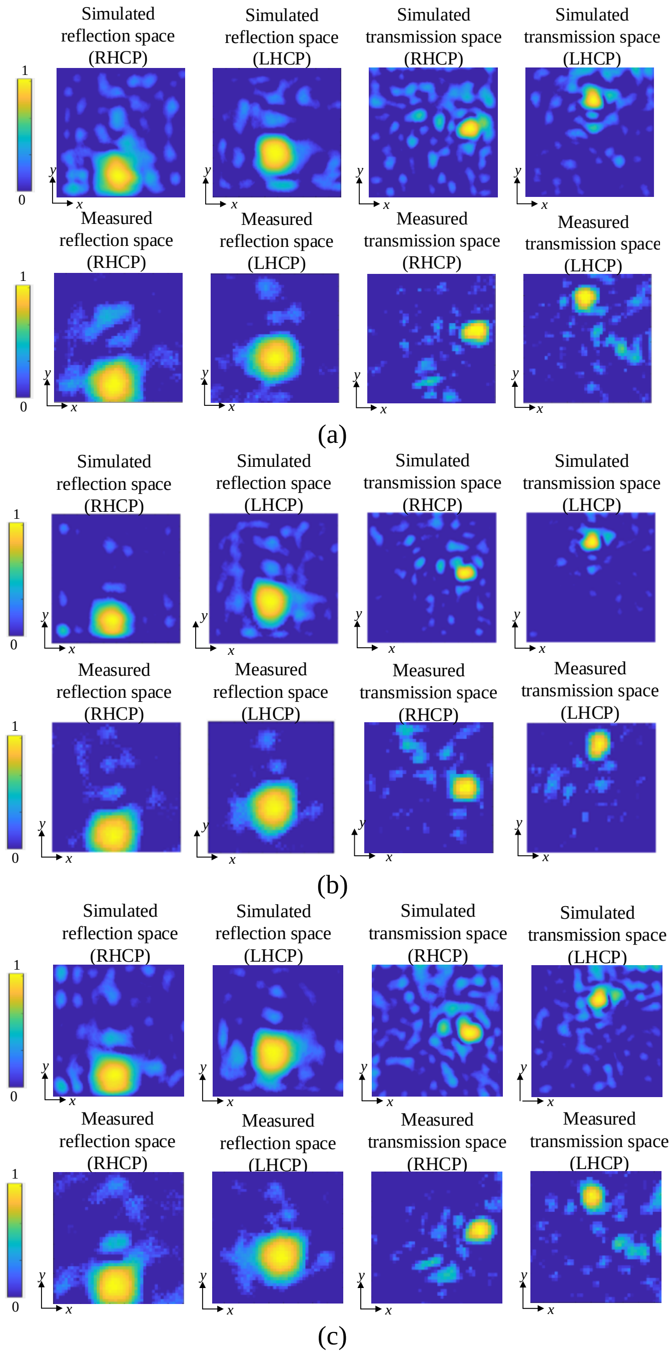

Fig. 16. Simulated and measured intensity (normalized) of LHCP and RHCP channels in the transmitting space and reflecting space. The observation plane is set at 150 mm and 50 mm from the MS for the reflecting and transmitting spaces, respectively. (a) 28.5 GHz. (b) 29 GHz. (c) 30 GHz.

some degradation compared with an ideal dount-liked intensity. As aforementioned, since the length of the receiving antenna is varied, resulting in the impedance matching deteriorating, the amplitude distribution fluctuated, especially at the edge frequency of the operating band. Therefore, the overall performance of the MS will be affected to some extent.

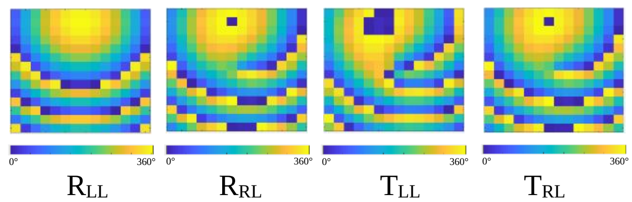

(a)

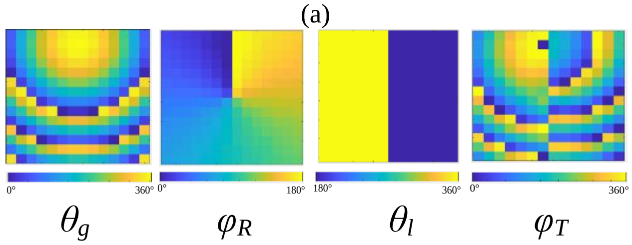

(b)

Fig. 17. (a) Compensating phase masks of R_{LL}, R_{RL}, T_{LL} and T_{RL} channels. (b) Phase masks of θ_g, φ_R, θ_l, φ_T .

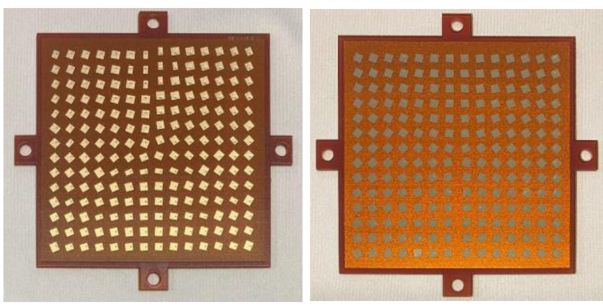

(a) (b)

Fig. 18. (a) Front view of the sample. (b) Back view of the sample.

The second MS focuses EM waves in four channels at different positions. The focal points are set as (x=0mm, y=20mm, and z=150mm) for R_{LL} channel, (x=0mm, y=40mm, and z=150mm) for R_{RL} channel, (x=30mm, y=0mm, and z=-50mm) for T_{LL} channel, (x=0mm, y=30mm, and z=-50mm) for T_{RL} channel. Therefore, the phase profile of R_{LL}, R_{RL}, T_{LL}, and T_{RL} can be respectively expressed as:

$$R_{LL}(x,y) = k\cdot\vec{R_i} + k\cdot\vec{Rd}_{LLi} \,. \tag{18}$$

$$R_{RL}(x,y) = k\cdot\vec{R_i} + k\cdot\vec{Rd}_{RLi} \,. \tag{19}$$

$$T_{LL}(x,y) = k\cdot\vec{R_i} + k\cdot\vec{Td}_{LLi} \,. \tag{20}$$

$$T_{RL}(x,y) = k\cdot\vec{R_i} + k\cdot\vec{Td}_{RLi} \,. \tag{21}$$

Rd_{LLi}, Rd_{RLi}, Td_{LLi}, and Td_{RLi} represent the distance between the i^{th} element and the focal point for the R_{LL}, R_{RL}, T_{LL}, and T_{RL} channels, respectively. The phase masks of R_{LL}, R_{RL}, T_{LL}, and T_{RL} channels are shown in Fig.14 (a). The corresponding phase masks of θ_g, φ_R, θ_l, φ_T are shown in Fig. 14 (b). The prototype is shown in **Fig.** 15. The simulated and measured intensity profile of transmitted and reflected LHCP and RHCP channels are given in **Fig.** 16. The simulated and measured results agree well. The waves in the four channels are focused on the different predesigned positions, respectively.

B. RHCP Input

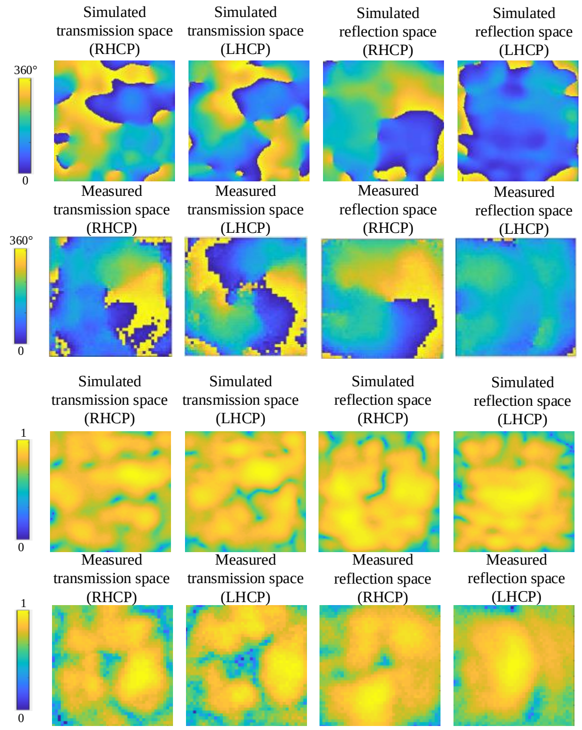

(a)

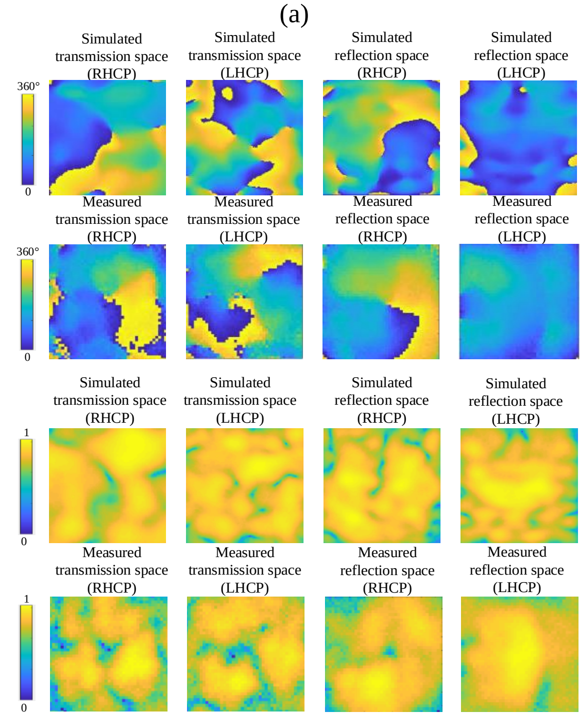

(b)

Fig. 19. Simulated and measured phase and intensity profiles (normalized) of LHCP and RHCP channels in the transmitting and reflecting spaces. (a) 29 GHz. (b) 29.5 GHz.

A MS achieving independent wavefront control of LHCP and RHCP channels in the reflecting and transmitting space under RHCP incident wave is also designed. The MS generates OAM with different topological charges (l), Specifically, l=0,1,2,1 for the R_{LR}, R_{RR}, T_{LR} and T_{RR} channels, respectively. The phase

TABLE II

COMPARISON OF DIFFERENT MSS FOR FULL-SPACE MULTI-CHANNEL BEAM-SHAPING

Ref.	**Configuration**	**Frequency**	**Polarization (input)**	**Polarization (Independent phase modulation)**	**Phase modulation methods**	**Fabrication**
[19]	Cascade metal sheets	25-35 GHz	*x*-polarization	*x*-polarization (reflection) *y*-polarization (transmission)	dynamic phase	PCB
[45]	Dielectric pillar	650 nm	RHCP	LHCP (reflection) RHCP (transmission)	P-B phase + Multipolar interference	Electron beam lithography (EBL)
[46]	Cascade metal sheets	14-16 GHz	*x*-polarization *y*-polarization	*y*-polarization (reflection) *x*-polarization (transmission)	dynamic phase	PCB
[47]	Cascade metal sheets	10-13 GHz	*x*-polarization *y*-polarization	*x*-polarization (reflection) *y*-polarization (transmission)	dynamic phase (Programmable)	PCB
[48]	Cascade metal sheets	9GHz	*x*-polarization *y*-polarization	*x*-polarization (reflection) *y*-polarization (transmission)	dynamic phase	PCB
[49]	Cascade metal sheets	8-9 GHz	*y*-polarization	*y*-polarization (reflection) *y*-polarization (transmission)	dynamic phase (Programmable)	PCB
[50]	Single-layer metal sheet	8-32 GHz	LHCP	LHCP (reflection) RHCP (transmission)	P-B phase	PCB
This work	Multi-layer metal sheets	28-30 GHz	LHCP or RHCP	LHCP (reflection) RHCP (reflection) LHCP (transmission) RHCP (transmission)	P-B phase, dynamic phase, chirality phase	Multi-material 3-D printing

profile of R_{LL}, R_{RL}, T_{LL}, and T_{RL} can be respectively expressed as:

$$R_{LR}(x,y) = k \cdot \vec{R}_i + 0 \cdot \varphi . \quad (22)$$

$$R_{RR}(x,y) = k \cdot \vec{R}_i + 1 \cdot \varphi . \quad (23)$$

$$T_{LR}(x,y) = k \cdot \vec{R}_i + 2 \cdot \varphi . \quad (24)$$

$$T_{RR}(x,y) = k \cdot \vec{R}_i + 1 \cdot \varphi . \quad (25)$$

The phase masks of R_{LR}, R_{RR}, T_{LR}, and T_{RR} channels are shown in Fig. 17 (a). Based on equations (3-2) and (7-2), the φ_R, θg, θ_l, φ_T can be calculated using the following equations:

$$\varphi_R(x,y) = R_{LR}(x,y) . \quad (26)$$

$$\varphi_R(x,y) - 2 \cdot \theta_g(x,y) = R_{RR}(x,y) . \quad (27)$$

$$\varphi_T(x,y) + \theta_l(x,y) = T_{RR}(x,y) . \quad (28)$$

$$\varphi_T(x,y) - \theta_l(x,y) - 2 \cdot \theta_g(x,y) = T_{LR}(x,y) . \quad (29)$$

The corresponding phase masks of θg, φ_R, θ_l, φ_T are shown in Fig. 17 (b). The fabricated prototype is shown in Fig. 18. The simulated and measured phases of LHCP and RHCP channels in the transmitting space and reflecting space are shown in Fig. 19. The measured results agree with the simulated ones. The topological charges are 1, 2, 1, and 0 for the transmitted co-polarization, transmitted cross-polarization, reflected cross-polarization, and reflected co-polarization, respectively. The corresponding mode purities at 29 GHz are 85%, 84%, 88%, and 84%, respectively.

Though many spin-decoupled MS have been developed for various applications by combining the geometric and dynamic phases, these MS are only limited to transmitting or reflecting spaces [28-42]. The demonstrated TRI spin decoupled full space MS doubles the information capacity and the beam coverage area. Compared with the transmitting-type metasurface, where some reflection is inevitable and wasted, the MS can fully use the energy of the incident wave with each of the four channels using a quarter of the incident energy. Compared with PCB technology, 3-D printing used here shows some advantages in terms of fabrication time, cost, design freedom, and waste. The printing time will not increase much when the layer increases. In contrast, much more time will be used in multi-layer PCB fabrication as each layer is fabricated independently and bonded together. In addition, the structure can be built in an additive rather than a subtractive manner. Therefore, the waste is less compared with the PCB fabrication. More importantly, the distance between adjacent layers can be flexibly selected in 3D printing, giving designers more design freedom. It is also worth mentioning that because acrylate inks are lossy, some energy will be dissipated in the printed dielectric substrate. Assuming no loss from the dielectric inks, the transmission magnitude in each channel improves by 0.05 on average.

Table II also compares different full-space multi-channel beam-shaping MSs. Most previous work uses different orthogonal incident waves to illuminate the MS to achieve full-space multi-channel beam shaping. To the author's knowledge, this is the first time that the MS is demonstrated to simultaneously and independently control the LHCP and RHCP channels in transmitting and reflecting spaces for a single CP incident wave. Nevertheless, the quadruplex phase modulation scheme results in amplitude fluctuation in some meta-atoms. Manipulating the amplitude response of the MS will be valuable for future work.

IV. Conclusion

3-D printed TRI MSs are demonstrated, which independently control the phase of co- and cross-polarization channels in the reflecting and transmitting spaces for a CP incident wave. For verification, the MSs achieve quadruplex channel OAM and focus under LHCP and RHCP incident waves, which are designed, fabricated, and measured. The multi-layered MS can be fabricated using the 3-D printing technique. The TRI polarization-multiplexed MS doubles the information capacity and the beam coverage area compared with state-of-the-art transmitting-only and reflecting-only MSs, paving the way to multifunctionality integration for future TRI RIS systems.

Acknowledgment

Nano Dimension supported this work under the collaboration between UTS and Nano Dimension. The authors would like to thank the engineering team at Nano Dimension, and the team from UTS ProtoSpace for their technical support. Special thanks to Jiexin Lai for the assistance during the metasurface measurement.

References

[1] F. Aieta, M. Kats, P. Genevet, F. Capasso, " Multiwavelength achromatic metasurfaces by dispersive phase compensation," *Science*, 347, 6228, Feb. 2015.
[2] A. Roy, Y. Naresh, A. Padmanabhan, A. Chockalingam and K. J. Vinoy, "Digitally reconfigurable metasurface array for a multipath based wireless link with media-based modulation," *IEEE Trans. Microw. Theory Techn*, vol. 70, no. 12, pp. 5418-5426, Dec. 2022.
[3] K. Zhang, Y. Wang, S. N. Burokur and Q. Wu, "Generating dual-polarized vortex beam by detour phase: from phase gradient metasurfaces to metagratings," *IEEE Trans. Microw. Theory Techn*., vol. 70, no. 1, pp. 200-209, Jan. 2022.
[4] J. Y. Dai et al., "Wireless communication based on information metasurfaces," *IEEE Trans. Microw. Theory Techn*., vol. 69, no. 3, pp. 1493-1510, Mar. 2021.
[5] H. Xue et al., "Multitarget wireless power transfer system using metasurface for quasi-bessel beams with large half power beam length," *IEEE Trans. Microw. Theory Techn*, vol. 70, no. 10, pp. 4449-4462, Oct. 2022.
[6] Y. Wei et al., "A multiband, polarization-controlled metasurface absorber for electromagnetic energy harvesting and wireless power transfer," *IEEE Trans. Microw. Theory Techn*, vol. 70, no. 5, pp. 2861-2871, May 2022.
[7] C. Wang, J. Zhang, S. Bai, X. Zhu and Z. Zheng, "A harmonic suppression energy collection metasurface insensitive to load and input power for microwave power transmission," *IEEE Trans. Microw. Theory Techn*, vol. 70, no. 8, pp. 4036-4044, Aug. 2022.
[8] J. Zhu, Y. Yang, M. Li, D. McGloin, S. Liao, J. Nulman, F. Iacopi, "Additively manufactured millimeter-wave dual-band single-polarization shared aperture Fresnel zone plate metalens antenna," *IEEE Trans. Antennas Propag*., vol. 69, no. 10, pp. 6261-6272, Oct. 2021.
[9] C.W. Qiu, T. Zhang, G. Hu, Y. Kivshar, "Quo vadis, metasurfaces?." *Nano Lett*., 21(13): 5461-5474, Jan. 2021.
[10] F. Qin, L. Ding, L. Zhang et al., "Hybrid bilayer plasmonic metasurface efficiently manipulates visible light." *Sci. Adv*. 2, e1501168, Jan. 2016.
[11] A. M. Shaltout, K. G. Lagoudakis, J. van de Groep, S. J. Kim, J. Vuckovic, V. M. Shalaev, M. L. Brongersma, "Spatiotemporal light control with frequency-gradient metasurfaces, " *Science*, 365, 374, Jul, 2019.
[12] M. Khorasaninejad, F. Capasso, "Metalenses: Versatile multifunctional photonic components," *Science* 358, eaam8100, Dec. 2017,.
[13] T. H. -Y. Nguyen and G. Byun, "A suboptimal approach to huygens' metasurfaces for wide-angle refraction," *IEEE Trans. Microw. Theory Techn*, vol. 70, no. 5, pp. 2588-2598, May. 2022.
[14] M. Chen, Y. Wu, L. Feng, Q. Fan, M. Lu, T. Xu, D. Tsai, "Principles, functions, and applications of optical meta-lens." *Adv. Opt. Mater*, 9(4): 2001414. 2021.
[15] W. T. Chen, et al. "A broadband achromatic metalens for focusing and imaging in the visible, " *Nat. Nanotechnol*, 2018, 13(3): 220-226.
[16] Y. Kato and A. Sanada, "Extraordinary transmission by double-sided hyperbolic metasurfaces with Γ -point degeneration at millimeter-wave bands," *IEEE Trans. Microw. Theory Techn*, vol. 67, no. 8, pp. 3297-3305, Aug. 2019.
[17] L. Li, P. Zhang, F. Cheng, M. Chang, and T. J. Cui, "An optically transparent near-field focusing metasurface," *IEEE Trans. Microw. Theory Techn*., vol. 69, no. 4, pp. 2015-2027, Apr. 2021.
[18] J. Zhu, Y. Yang, J. Lai, J. Nulman, "Additively manufactured polarization insensitive broadband transmissive metasurfaces for arbitrary polarization conversion and wavefront shaping, " *Adv. Opt. Mater*, 10(21): 2200928, Aug. 2022.
[19] Y. Wang et al., "Broadband high-efficiency ultrathin metasurfaces with simultaneous independent control of transmission and reflection amplitudes and phases," *IEEE Trans. Microw. Theory Techn.*, vol. 70, no. 1, pp. 254-263, Jan. 2022.
[20] H. Zhou, et al. "Polarization-encrypted orbital angular momentum multiplexed metasurface holography" *ACS nano*, 14(5): 5553-5559, 2020.
[21] X. Wu et al., "Multitarget wireless power tansfer system strategy based on metasurface-holography multifocal beams," *IEEE Trans. Microw. Theory Techn*, doi: 10.1109/TMTT.2023.3260401.
[22] I. Javed et al. "Broad-band polarization-insensitive metasurface holography with a single-phase map, " *ACS Appl. Mater. Interfaces*, 14(31): 36019-36026, 2022.
[23] G. Zheng, "Metasurface holograms reaching 80% efficiency," *Nat. Nanotechnol*, 10(4): 308-312, 2015.
[24] L. Huang, S. Zhang, and T. Zentgraf. "Metasurface holography: from fundamentals to applications." *Nanophotonics* 7.6. 1169-1190, 2018.
[25] Y. Yuan, Q. Wu, S. N. Burokur and K. Zhang, "Chirality-assisted phase metasurface for circular polarization preservation and independent hologram imaging in microwave region," *IEEE Trans. Microw. Theory Techn*, doi: 10.1109/TMTT.2023.3256527.
[26] L. Li et al. "Electromagnetic reprogrammable coding-metasurface holograms.," *Nat. Commun*, 8(1): 197, Aug.2017.
[27] W. Ye, et al. "Spin and wavelength multiplexed nonlinear metasurface holography." *Nat. Commun*, 7.1 11930 Jan.2016.
[28] J. Li, Y. Yuan, G. Yang, et al. "Hybrid dispersion engineering based on chiral metamirror." *Laser Photon. Rev*., 17(3): 2200777.
[29] L. Wang, H. Shi, X. Chen, B. Qu, J. Yi, A. Zhang, Z. Xu, and H. Liu, "Multibeam metasurface antenna enabled by orbital angular momentum demultiplexing feeding for IoT communication," *IEEE Internet Things J*., vol. 10, no. 18, pp. 16169-16182, Sep. 2023.
[30] K. Zhang, Y. Yuan, X. Ding, B. Ratni, S. N. Burokur, Q. Wu. "High-efficiency metalenses with switchable functionalities in microwave region, " *ACS Appl. Mater. Interfaces*, 11, 28423-28430, Jun. 2019.
[31]Y. Yuan, K. Zhang, X. Ding, B. Ratni, S. N. Burokur, Q. Wu, "Complementary transmissive ultra-thin meta-deflectors for broadband polarization-independent refractions in the microwave region "*Photonics Res*. 7, Jun. 2019.
[32] W.L. Guo, et al. "Ultrawideband spin-decoupled coding metasurface for independent dual-channel wavefront tailoring, " *Ann. Phys*., 532(3): 1900472 Feb. 2020.
[33] J. Zhu, Y. Yang, J. Lai and M. Li, "3-D printed noninterleaved reflective metasurfaces supporting dual-band spin-decoupled quadruplex channel

independent beam-shaping with controllable energy distribution," *IEEE Trans. Microw. Theory Techn*, doi: 10.1109/TMTT.2023.3308165.
[34] Z. Jiang, F. Wu, T. Yue, W. Hong, " Wideband and low-profile integrated dual-circularly-polarized transmit-arrays enabled by antenna-filter-antenna phase shifting cells," *IEEE Trans. Antennas Propag*, 69(11), 7462-7475, 2021.
[35] J. Zhu, Y. Yang, N. Hu, S. Liao, J. Nulman, "Additively manufactured multi-material ultrathin metasurfaces for broadband circular polarization decoupled beams and orbital angular momentum generation." *ACS Appl. Mater. Interfaces* 13.49 59460-59470, Dec. 2021.
[36] X. Guo, et al. "Metasurface-assisted multidimensional manipulation of a light wave based on spin-decoupled complex amplitude modulation." *Opt. Lett* 47.2: 353-356, 2022.
[37] H. Xu, L. Han, Y. Li, Y. Sun, J. Zhao, S. Zhang, C.-W. Qiu, "Completely spin-decoupled dual-phase hybrid metasurfaces for arbitrary wavefront control, " *ACS Photonics*, 6, 211, Jan. 2019.
[38] G. Ding, K. Chen, G. Qian, J. Zhao, T. Jiang, Y. Feng, Z. Wang "Independent energy allocation of dual helical multi-beams with spin-selective transmissive metasurface," *Adv. Opt. Mater.*, 8(16): 2000342, May. 2020.
[39] Y. Xu, Q. Li, X. Zhang, M. Wei, Q. Xu, Q.Wang, H. Zhang, W.Zhang, C. Hu, Z. Zhang, C. Zhang, X. Zhang, J. Han, and W. Zhang "Spin-decoupled multifunctional metasurface for asymmetric polarization generation, " *ACS Photonics*, 6(11): 2933-2941, Oct. 2019.
[40] Y. Yuan, K. Zhang, B. Ratni, Q. H. Song, X. M. Ding, Q. Wu, S. N.Burokur, P. Genevet, "Independent phase modulation for quadruplex polarization channels enabled by chirality-assisted geometric-phase metasurfaces, " *Nat. Commun.*, 11, 4186, Aug. 2020.
[41] Y. Yuan, Q. Wu, S. N. Burokur and K. Zhang, "Chirality-assisted phase metasurface for circular polarization preservation and independent hologram imaging in microwave region," *IEEE Trans. Microw. Theory Techn*, vol. 71, no. 8, pp. 3259-3272, Aug. 2023, doi: 10.1109/TMTT.2023.3256527.
[42] J. Zhu, M. Li, J. Lai, et al. "Multimaterial additively manufactured transmissive spin-decoupled polarization-maintaining metasurfaces, " *Laser Photon. Rev*., 2023: 2300433.
[43] Y. Saifullah, Y. He, A. Boag, G.M. Yang, F.Xu. "Recent Progress in Reconfigurable and Intelligent Metasurfaces: A Comprehensive Review of Tuning Mechanisms, Hardware Designs, and Applications, " *Adv. Sci*., 2203747, Nov. 2022
[44] Z. Li, Q. Dai, M. Q. Mehmood, G. Hu, B. L. Yanchuk, J. Tao, C. Hao, I. Kim, H. Jeong, G. Zheng, S. Yu, A. Alù, J. Rho, C.-W. Qiu,: "Full-space cloud of random points with a scrambling metasurface, " *Light Sci. Appl*., 7, 63, Sep. 2018.
[45] J. Sung, G.-Y. Lee, C. Choi, J. Hong, B. Lee, "Single-layer bifacial metasurface: full-space visible light control, " *Adv. Opt. Mater*. 2019, 7,1801748.
[46] L. Zhang, R. Y. Wu, G. D. Bai, H. T. Wu, Q. Ma, X. Q. Chen, T. J. Cui, "Transmission-reflection-integrated multifunctional coding metasurface for full-space controls of electromagnetic waves," *Adv. Funct. Mater*. 28, 1802205, Jan. 2018.
[47] L. Bao, Q. Ma, R.Y. Wu, X. Fu, J. Wu, T. J. Cui, "Programmable reflection-transmission shared-aperture metasurface for real-time control of electromagnetic waves in full space, "*Adv. Sci*., 8(15): 2100149, May, 2021.
[48] Y. Zhuang, G. Wang, T. Cai, Q. Zhang, "Design of bifunctional metasurface based on independent control of transmission and reflection," *Opt. Express*, 26, 3594, Feb. 2018.
[49] R.Y. Wu, L. Zhang, L. Bao, L. W. Wu, Q. Ma, G. D. Bai, H. T. Wu, Tie Jun Cui, "Digital metasurface with phase code and reflection-transmission amplitude code for flexible full-space electromagnetic manipulations, " *Adv. Opt. Mater*, 7(8): 1801429, Jan, 2019.
[50] M. R. Akram, G. Ding, K. Chen, Y. Feng, W. Zhu, "Ultrathin single layer metasurfaces with ultra‐wideband operation for both transmission and reflection, " *Adv. Mater*, 32(12): 1907308, Feb. 2020.
[51] X. Mu, Y. Liu, L. Guo, J. Lin and R. Schober, "Simultaneously transmitting and reflecting (STAR) RIS aided wireless communications," *IEEE Trans. Wireless Commun*., vol. 21, no. 5, pp. 3083-3098, May 2022, doi: 10.1109/TWC.2021.3118225.
[52] A. Papazafeiropoulos, A. M. Elbir, P. Kourtessis, I. Krikidis and S. Chatzinotas, "Cooperative RIS and STAR-RIS assisted mMIMO communication: analysis and optimization," *IEEE Trans. Veh. Technol*, doi: 10.1109/TVT.2023.3264724.
[53] C. Wu, X. Mu, Y. Liu, X. Gu and X. Wang, "Resource allocation in STAR-RIS-aided networks: OMA and NOMA," *IEEE Trans. Wireless Commun*., vol. 21, no. 9, pp. 7653-7667, Sept. 2022.
[54] W. Ni, Y. Liu, Y. C. Eldar, Z. Yang and H. Tian, "STAR-RIS integrated nonorthogonal multiple access and over-the-air federated learning: framework, analysis, and optimization," *IEEE Internet Things J*, vol. 9, no. 18, pp. 17136-17156, 15 Sept.15, 2022.

Jianfeng Zhu (Member, IEEE) received the B.Eng. degree in communication engineering from Beijing University of Posts and Telecommunications (BUPT), Beijing, China and Ph. D. degree from BUPT and University of Technology Sydney (UTS), Ultimo, NSW, Australia. He is now with South China University of Technology. His research interests include millimeter-wave and terahertz antennas and metasurfaces. He is looking for collaborators.

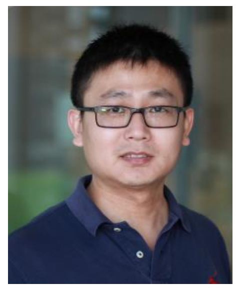

Yang Yang (Senior Member, IEEE) was born in Bayan Nur, Inner Mongolia, China and received the PhD degree in Electronic Engineering from Department of Electrical and Computer Systems Engineering, Monash University, Melbourne, Australia, in 2013.

Dr Yang was with the State Key Laboratory of Terahertz and Millimeter Waves, City University of Hong Kong, in 2016. Since December 2016, he joined the University of Technology Sydney (UTS), Australia. He is currently an Associate Professor and a Group Leader of 3D Millimetre-Wave and Terahertz Circuits and Antennas in UTS Tech Lab. His research interests include emerging RF materials and additive manufacturing techniques for 3D millimetre-wave and terahertz device designs for 5G and biomedical applications. He has over 200 international publications in microwave, millimetre-wave and terahertz circuits and antennas. In 2021, Dr Yang received the Linkage Infrastructure, Equipment and Facilities (LIEF) Award funded by the Australian Research Council to establish the national laboratory of Australian 3D Terahertz Beam Measurement Platform (500 GHz). Dr Yang is a current Associate Editor of *IEEE Transactions on Microwave Theory and Techniques* (from 2022). He is the Chair of IEEE MTT-S Education Resources Development (2023), and Chair of IEEE NSW AP-S/MTT-S Joint Chapter (2023).